

ORIGINAL ARTICLE

Open Access

Grating-based x-ray dark-field CT for lung cancer diagnosis in mice



Peiyuan Guo^{1,2,3}, Li Zhang^{1,2,3}, Jincheng Lu^{1,2,3}, Huitao Zhang⁴, Xiaohua Zhu^{1,2}, Chengpeng Wu^{1,2}, Xiangwen Zhan⁵, Hongxia Yin⁶, Zhenchang Wang⁶, Yan Xu^{6*} and Zhentian Wang^{1,2,3*} 

Abstract

Background The low absorption of x-rays in lung tissue and the poor resolution of conventional computed tomography (CT) limits its use to detect lung disease. However, x-ray dark-field imaging can sense the scattered x-rays deflected by the structures being imaged. This technique can facilitate the detection of small alveolar lesions that would be difficult to detect with conventional CT. Therefore, it may provide an alternative imaging modality to diagnose lung disease at an early stage.

Methods Eight mice were inoculated with lung cancers simultaneously. Each time two mice were scanned using a grating-based dark-field CT on days 4, 8, 12, and 16 after the introduction of the cancer cells. The detectability index was calculated between nodules and healthy parenchyma for both attenuation and dark-field modalities. High-resolution micro-CT and pathological examinations were used to crosscheck and validate our results. Paired *t*-test was used for comparing the ability of dark-field and attenuation modalities in pulmonary nodule detection.

Results The nodules were shown as a signal decrease in the dark-field modality and a signal increase in the attenuation modality. The number of nodules increased from day 8 to day 16, indicating disease progression. The detectability indices of dark-field modality were higher than those of attenuation modality ($p=0.025$).

Conclusions Compared with the standard attenuation CT, the dark-field CT improved the detection of lung nodules.

Relevance statement Dark-field CT has a higher detectability index than conventional attenuation CT in lung nodule detection. This technique could improve the early diagnosis of lung cancer.

Key points

- Lung cancer progression was observed using x-ray dark-field CT.
- Dark-field modality complements with attenuation modality in lung nodule detection.
- Dark-field modality showed a detectability index higher than that attenuation in nodule detection.

Keywords Disease progression, Early detection of cancer, Lung diseases, Tomography (x-ray computed), X-rays

*Correspondence:

Yan Xu

yanxu@ccmu.edu.cn

Zhentian Wang

wangzhentian@tsinghua.edu.cn

Full list of author information is available at the end of the article



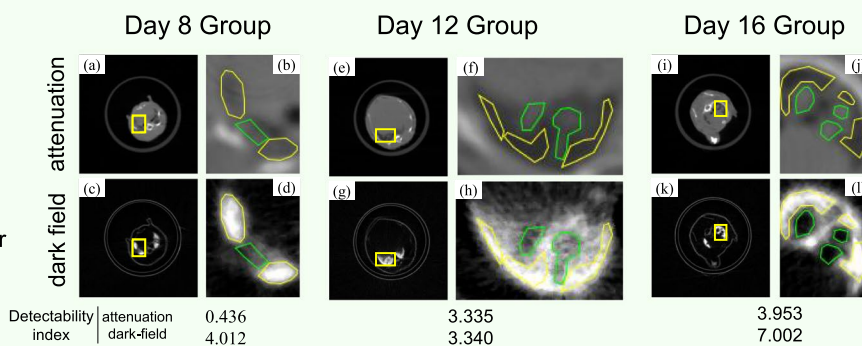
© The Author(s) 2024. **Open Access** This article is licensed under a Creative Commons Attribution 4.0 International License, which permits use, sharing, adaptation, distribution and reproduction in any medium or format, as long as you give appropriate credit to the original author(s) and the source, provide a link to the Creative Commons licence, and indicate if changes were made. The images or other third party material in this article are included in the article's Creative Commons licence, unless indicated otherwise in a credit line to the material. If material is not included in the article's Creative Commons licence and your intended use is not permitted by statutory regulation or exceeds the permitted use, you will need to obtain permission directly from the copyright holder. To view a copy of this licence, visit <http://creativecommons.org/licenses/by/4.0/>.

Graphical Abstract

Grating-based x-ray dark-field CT for lung cancer diagnosis in mice



- The nodules were shown as a signal decrease in the dark-field modality and a signal increase in the attenuation modality.
- The detectability indices of dark-field modality were higher than those of attenuation modality ($p = 0.025$) in lung nodule detection.



Typical slices of attenuation and dark-field modality of the day 8 (a-d), day 12 (e-h), and day 16 (i-l) groups. For each group, ROIs of nodules and normal parenchyma were selected, and detectability indices of the two modalities were calculated.

Dark-field CT has a higher detectability index than conventional attenuation CT in lung nodule detection. This technique could improve the early diagnosis of lung cancer.



**Eur Radiol Exp (2024) Guo P, Zhang L, Lu J et al;
DOI: 10.1186/s41747-023-00399-w**

Background

Lung diseases such as chronic obstructive pulmonary disease and lung cancer are common causes of death worldwide [1–5]. X-ray radiography and computed tomography (CT) are noninvasive tools to diagnose lung disease. In radiography, images are generated based on the differential attenuation of x-rays with different tissue densities. However, due to the limited spatial resolution of the CT and the poor attenuation of x-ray in lung tissue, the standard CT technique cannot always detect small structural changes in the pulmonary alveoli [4, 6] and very small lung tumors [7, 8]. Therefore, early diagnosis of lung diseases like emphysema can only be done by observing the slight signal change of attenuation caused by structural change of alveoli parenchyma [9].

Grating-based x-ray dark-field imaging utilizes x-ray's wave character [10–13] and detects the perturbation of the wavefront of x-rays. It measures the phase contrast signal (representing refraction) and dark-field signal (representing small angle scattering) caused by an object [14]. Although lung tissue tends to have low x-ray attenuation, the alveoli have strong scattering properties [15, 16]. As a result, grating-based x-ray dark-field imaging can identify pathological changes within the lung that

generate a strong dark-field signal [15–18] and could be used to identify lung diseases at an early stage.

Dark-field imaging has already been experimentally used to assess bones, brain, microcalcifications, and lungs in humans [17, 19–23]. Scherer et al. [24] compared *in vivo* dark-field radiography with standard attenuation radiography in a lung cancer mouse model and found that x-ray dark-field imaging is far more suitable for nodule detection. Other studies have also found that dark-field imaging can improve the early detection of emphysema and fibrosis [6]. Furthermore, pathological changes in human lung could be differentiated with spectral dark-field radiography [25]. Velroyen et al. [26] conducted the first dark-field CT on mice and demonstrated that emphysema and fibrosis can be detected and classified with the cooperation of dark-field and attenuation modality. Furthermore, *in vivo* dark-field CT was also conducted to detect lung diseases in mice [27]. Apart from lung disease research on the scale of mice, a prototype of dark-field CT with a scale of humans has been recently developed [21], which carried forward the application of clinical diagnosis of lung diseases.

In this study, we aimed to evaluate the ability of the dark-field CT to detect pulmonary nodules in a mouse

lung cancer model at different stages of cancer development in relation to standard attenuation modality and micro-CT.

Methods

Preparation of the mouse models

This prospective study was approved by our institutional review board. All experiments were performed as per GB/T 35892-2018 Laboratory Animal-Guideline for ethical review of animal welfare.

For this study, 5-week-old male BALB/c (Hfk, Beijing, China) nude mice were used. The mice were housed in specific pathogen free rooms at a constant temperature of 20 to 26 °C and humidity of 40% to 70% with a 12-h light cycle. The mice were provided with food and water ad libitum. Lung cancer was introduced into the mice by injecting a 100 μ L (0.5×10^6 cells) solution of the B16 cell line (Institute of Laboratory Animals Science, Peking Union Medical College, Beijing, China) into the caudal vein [28]. The eight mice were injected simultaneously, and to eliminate the influence of inherent variations among different mice, each time two mice were randomly selected and scanned using a dark-field CT on days 4, 8, 12, and 16 after the introduction of the cancer cells.

For the autolysis study (details are given in dedicated subsections below), another four mice were used. The origin of these mice was the same as those mentioned above, except that they were not injected with cancer cells.

Grating-based dark-field CT

The dark-field signal is related to the strength of small-angle scattering. For porous objects, dark-field signal is generated by the microstructure containing the mass interfaces between the object and the air [29]. When exposed to x-rays, the lungs can cause a strong small-angle scattering at the pulmonary alveoli structure on the micron scale, thus creating a strong dark-field signal. In lung cancer, the porous alveoli structure is replaced by relatively denser and less scattering nodules, eventually leading to a decrease in the dark-field signal and an increase in the attenuation signal [24].

A standard grating interferometer setup with three gratings can be used to measure the dark-field signal, as shown in Fig. 1. The core of these three gratings is the beam splitter grating G1, which generates a periodic intensity fringe pattern at a certain distance behind G1, called the Talbot effect [13, 30]. Since the period of the fringes is much smaller than the pixel of the detector, the analyzer grating G2 is used to sample the fringe pattern by blocking part of the incoming x-rays. Since this method requires high coherence of the x-ray source, a source grating G0

can be placed right after the x-ray source to generate an array of line sources, each of which is partially coherent, and this G0 helps laboratory source to satisfy the coherence requirement [31]. The G2 grating moves step by step perpendicular to the fringe to absorb different parts of the fringe pattern, and the detector records the intensity at each step, forming an intensity curve relative to the steps called the phase stepping curve [14]. Fourier analysis is then applied to the phase stepping curve to calculate the fringe's mean intensity, phase, and visibility, which correspond to the three modalities of this imaging method.

If a sample is placed in the beam path, it will cause attenuation of the beam, leading to a reduction in the intensity, which is used in conventional imaging. Additionally, the small-angle scattering can be caused by the internal microstructures within the sample, leading to a reduction in the visibility of the fringes. The dark-field signal of a sample is defined as the visibility reduction and is calculated by taking the negative logarithm of the ratio between the visibility of the fringes with and without the sample.

As for the image reconstruction of dark-field signals, it has been shown that the dark-field signal follows the integral path rule of the exponential decay similar to the Beer-Lambert law [29, 32–34], which is also used on the standard attenuation CT. Therefore, by assuming that the dark-field signal is a rotational-invariant, the reconstruction methods used on the standard CT could also be used for the dark-field reconstruction. However, it is important to note that since the rotational invariance is not seen in many fibrous samples [35–37], this method can lead to artifacts.

Experimental setup

The experiments were conducted on the experimental setup developed by Tsinghua University. The setup consists of a flat panel detector with a pixel size of 75 μ m (DEXELA 2923, Varex Imaging Corporation, Salt Lake City, USA), an x-ray tube with a focal spot of 1.0 mm (MXR-160HP/11, Comet Group, Flamatt, Switzerland), and a set of Talbot-Lau grating interferometer [30]. The three gratings of the interferometer share the same silicon substrate material and the same 0.5-duty cycle. The bar material of G0 and G2 grating was gold, and that of the G1 grating was silicon. The heights of the bars were 47 μ m, 38.4 μ m, and 40 μ m for the G0, G1, and G2, respectively. All gratings had a period of 4.8 μ m. The G1 grating produces a phase shift of π . The distance between the adjacent gratings was set to approximately 0.695 m, using the fifth Talbot order.

Data acquisition

The mice were euthanized right before the experiment by injecting an overdose of ketamine (Beikang, Jiangxi, China) into the peritoneum. The mice were then fixed in a plastic centrifuge tube. Subsequently, the tube was placed on

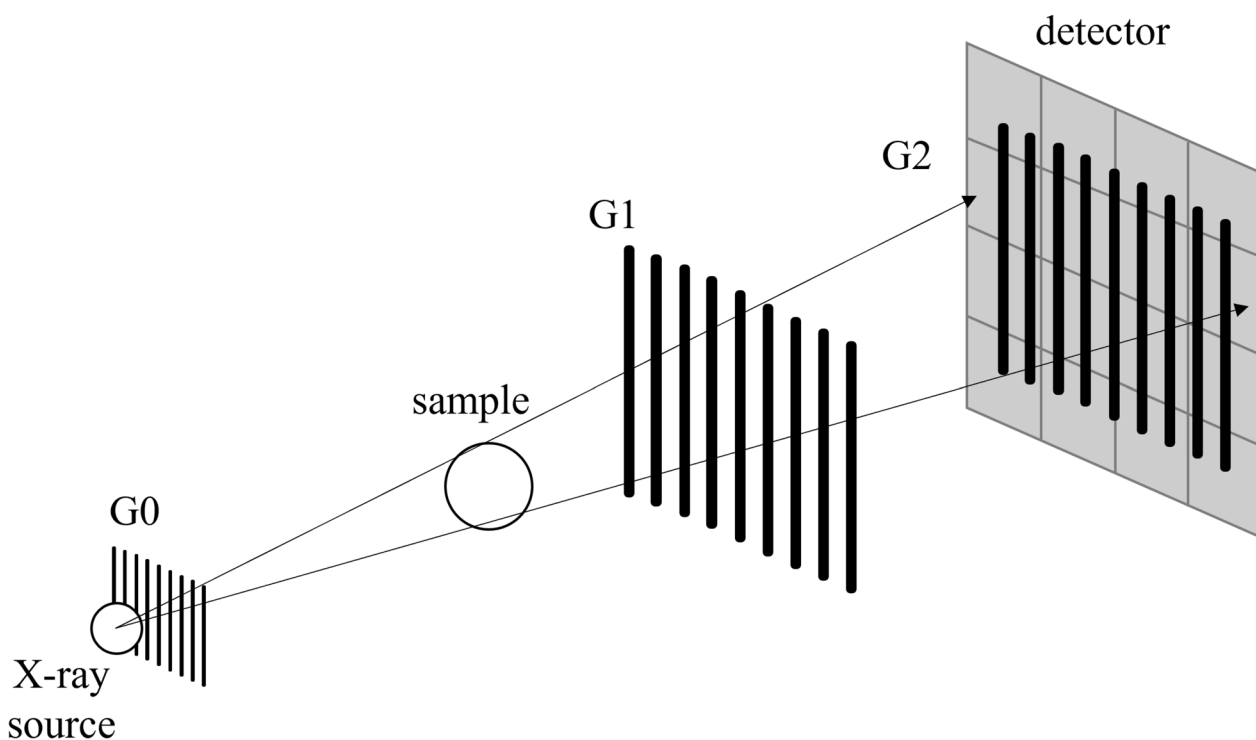


Fig. 1 Schematic diagram illustrating the positions of the three gratings of the interferometer. The source grating (G0), the beam splitter (G1), and the analyzer grating (G2) are placed in the beam path to modulate the wavefront

the rotation stage in an upright position. All images were acquired using a source voltage of 35 kVp and a current of 20 mA. The exposure time of the detector was set at 2,000 ms. Scanning was performed with a magnification factor of about $\times 1.35$. For each scan, 720 angular views were taken at an interval of 0.5° , covering the whole 360° . An 8-step phase stepping was conducted at each angular position. Due to the slow readouts of the detector and the overheads of mechanical moves of motors, the total scan time lasted approximately 8 h. Two set of background phase-stepping images were acquired before and after the rotation. These signals were then used to retrieve the signals from the former and latter half of the 720 angular positions.

Data processing and reconstruction

The three signals were retrieved by discrete Fourier transform, conducted on each set of phase-stepping images [14, 38]. After retrieval, fan-beam reconstruction can be applied to these three signals to obtain the tomographic images. Due to the tilt of the rotation axis, geometric calibration was necessary before performing the fan beam reconstruction. The exact tilt angle and position of the rotation axis were found through iterative optimization. The three signals were calibrated into a standard fan beam projection according to the position parameters of the rotation axis. Thereafter filtered back projection with a

Ram-Lak filter [39] was applied to reconstruct the attenuation and dark-field tomographic images. The CONRAD software [40] was used to reconstruct the projected data into 730 tomographic images with an 850×850 matrix, whose isotropic voxels' edge length is $70 \mu\text{m}$.

Micro-CT

The grating interferometer used in our study had a limited spatial resolution. In order to better visualize the lung cancers in the mice and cross-validate the results of the dark-field CT, micro-CT scans were performed on one of the mice in each group. The micro-CT was conducted on the HR-225CT (Capital Normal University, Beijing, China) using a voltage of 80 kVp and a current of $250 \mu\text{A}$. The focal size of the x-ray source in the setup was $8 \mu\text{m}$, and the pixel size of the planar detector was $139 \mu\text{m}$. The scanning was performed with a magnification factor of about $\times 13$. The projection data of 1,440 angular positions were reconstructed using the Feldkamp-Davis-Kress method [41] into 1,400 tomographic images with a $1,200 \times 1,200$ matrix, whose isotropic voxels' edge length was $15 \mu\text{m}$. The total acquisition time lasted approximately 26 min.

Quantitative analysis

We used the detectability index (d') [42–44] to quantitatively evaluate the feasibility of the modalities to detect

lung nodule from normal parenchyma. The detectability index is a metric for classification tasks that measures the overlap of the distribution of the two classes on the decision axis, and for an ideal observer, it can be expressed as [42]:

$$d'^2 = K^2 \int \frac{|F(v)|^2 M(v)^2}{N(v)} dv \quad (1)$$

where K is the large-area transfer ratio, $G(v)$ is the spatial frequency spectrum of the difference between the signal and background, $M(v)$ is the system modulation transfer function, and $N(v)$ is the noise power spectrum. However, since the modulation transfer function and noise power spectrum of our system are difficult to measure, we here use another expression to calculate d' [44]:

$$d' = \frac{\langle S \rangle_2 - \langle S \rangle_1}{\sqrt{\frac{1}{2}\sigma_1^2 + \frac{1}{2}\sigma_2^2}} \quad (2)$$

where $\langle S \rangle_1$ and σ_1 denotes the mean value and the standard deviation of class 1 and the same for subscript 2 and class 2. Specifically in our study, the class 1 and 2 represent the normal pulmonary parenchyma and nodules, respectively.

In order to measure the d' , regions of interest (ROI) have to be selected on CT slices for these two classes. The ROIs are supposed to contain all of the nodule and parenchyma in order to consider the biological variability. However, due to the lack of histological analysis, some areas on the CT slice cannot be definitely classified as nodule or parenchyma, so these areas were excluded and the ROIs were selected conservatively that only areas whose signals were strong in attenuation or dark-field were classified as nodule or parenchyma. Therefore, the detectability index measured here will be slightly higher than the true value since the biological variability was suppressed. After selected, the ROIs are median-filtered with a radius of 2 pixels before the d' calculation. The mean value and standard deviation are then measured for the nodule and normal parenchyma to calculate the d' .

Histology

Histology analysis was conducted to study the autolysis happened in mice's lung after death, whose detail will be given in dedicated subsection below. Another four mice (as mentioned above) were euthanized, and their lung tissues were dissected at 2, 4, 6, and 8 h postmortem. These lung tissues were fixed in 10% formalin solution (Damao, Tianjin, China). Paraffin sections were prepared with a thickness of 4 μm and then subjected to hematoxylin and eosin staining (Hushi, Shanghai, China). Then, the slices were dehydrated and scanned under microscope.

Statistical analysis

Statistical analysis was conducted using GraphPad Prism (Version 9.0.0, GraphPad Software Inc., USA). To prove dark-field's superiority to attenuation in nodule detection, whose detail will be given in dedicated subsection below, a paired t -test [45] was performed on the detectability index of dark-field and attenuation modalities measured on different samples. If the detectability index of dark-field modality is significantly higher than that of attenuation modality, then it can be proved that dark-field modality is better than attenuation in nodule detection.

Statistical analysis was also conducted to disprove the influence of autolysis, whose detail will be given in dedicated subsection below. An ROI was selected at the same position in the first and last dark-field projection signal from one experiment, and the dark-field signal of the pixels in these two projections were selected. The null hypothesis is that the signals in the last projection were lower than those in the first projection, which means our experiments were influenced by autolysis. One-sided paired t -test [45] was applied to these two groups of signals to test whether the null hypothesis is valid. If not, the impact of autolysis can be excluded.

Results

Dark-field and attenuation CT

Images acquired using the dark-field CT and micro-CT for one of the mice in each group are compared in Fig. 2. The CT results contain the typical tomographic slices of the standard attenuation and dark-field modalities and the vertical reslices according to the section profile shown in the tomographic slices. The micro-CT slices were used to account for the lack of spatial resolution in the standard attenuation modality. The micro-CT was manually matched with the dark-field CT. Note that the two samples in each group share the same results, so we selected one sample from each group and presented it here.

No lung nodule formation was noted on day 4 on any of the images. However, the number of nodules increased from day 8 to day 16, indicating disease progression. Generally, a signal increase in the attenuation modality corresponded with a signal decrease in the dark-field modality, indicating the nodules (yellow circle, Fig. 2), except for day 12, whereby an increase in the attenuation signal did not correspond with a decrease in the dark-field signal (dashed-line circle, Fig. 2).

The tumor characteristics in different stages of cancer progression were also studied. The number of nodules were counted according to both attenuation and dark-field data. The size of nodules was measured as per the Fleischner 2017 guideline [46]. In this guideline, the biggest section of a nodule is selected among transverse,

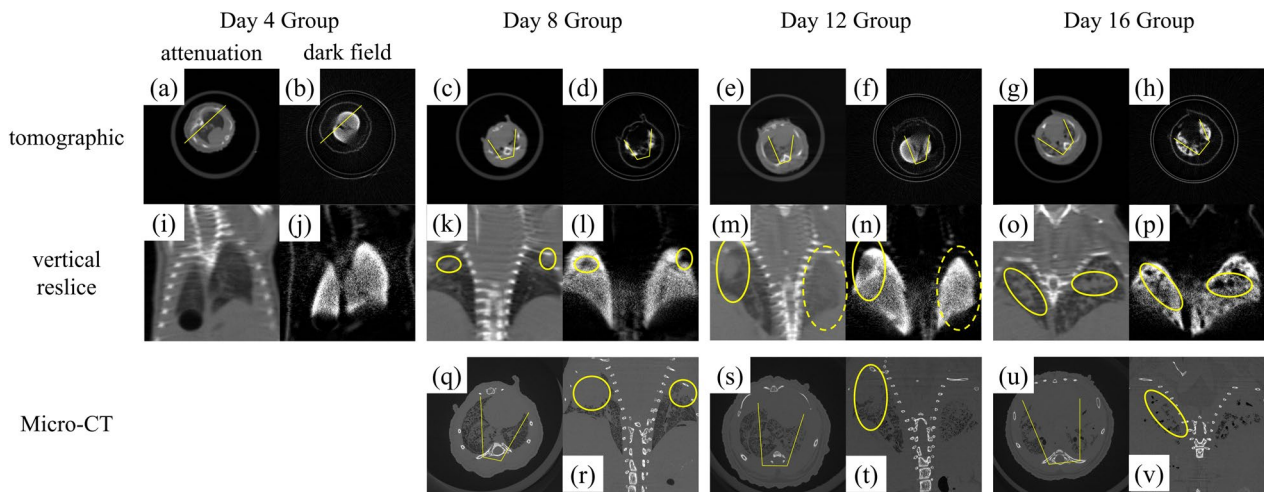


Fig. 2 Comparison of the standard attenuation and dark-field modalities and micro-computed tomography (micro-CT) for one of the mice in each group. Images from **a** to **h** illustrate the tomographic images, and images from **i** to **p** illustrate the vertical reslices for the standard attenuation and dark-field modalities. The greyscale window was set between (0, 1.5) for the standard attenuation modality and between (0, 8) for the dark-field modality. The vertical reslices were generated from the tomographic images according to the section profile indicated by the yellow line. The yellow circles indicate the lung nodule on the vertical reslices. Images from **q** to **v** illustrate the tomographic and vertical reslices of the micro-CT images acquired on days 8, 12, and 16

Table 1 Number and size of nodules in different groups

Group	Number of nodules	Size of nodules (mm)
Day 8	8	1.461 ± 0.200
Day 12	10	1.547 ± 0.252
Day 16	17	1.644 ± 0.491

The size of nodules is represented as the mean ± standard deviation

coronal, and sagittal reconstruction data, and the size of the nodule is represented by the average of the long and short axis diameters of the nodule’s biggest section. The number and average size of the nodules in different groups are listed in Table 1. It can be observed that the number of nodules increases with the progression of cancer, while the size of nodules only slightly increases.

Quantitative analysis

Generally, nodules have a low dark-field signal and high attenuation signal, and vice versa for normal pulmonary parenchyma. However, as shown by the line profile in Fig. 3, the contrast between the nodule and normal tissue was higher in the dark-field modality than that in the standard attenuation modality.

To measure the detectability index, ROIs of normal parenchyma and nodules were selected, as shown in Fig. 4, and the d' was calculated according to Eq. 2, as shown in Table 2. Overall, the dark-field modality showed a higher detectability index than the standard attenuation modality, especially in day 8.

Following the same calculation method, the detectability indices of all the mice with observable nodules are listed in Table 3, including groups from day 8 to day 16.

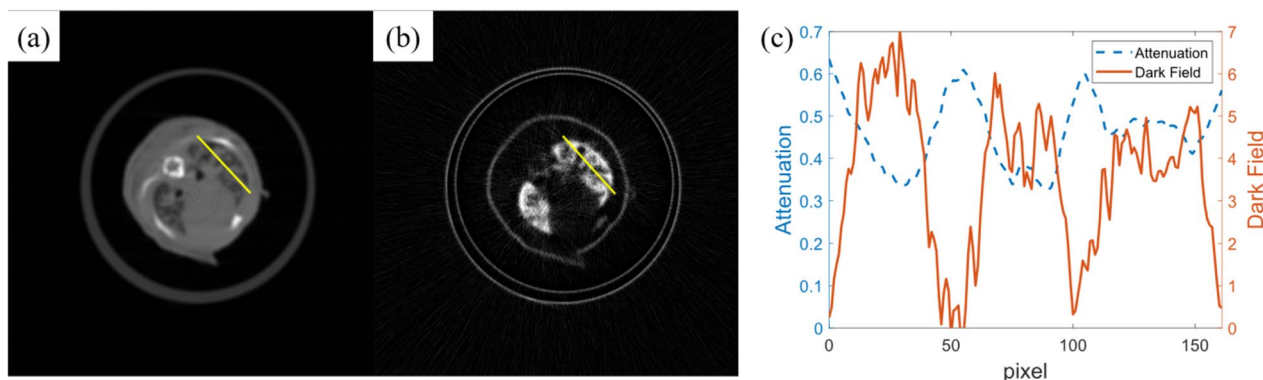


Fig. 3 A typical tomographic slice of attenuation (a) and dark-field modality (b) obtained from one of the samples in the day 16 group. c The attenuation and dark-field profile for the pixels indicated by the yellow line in a and b

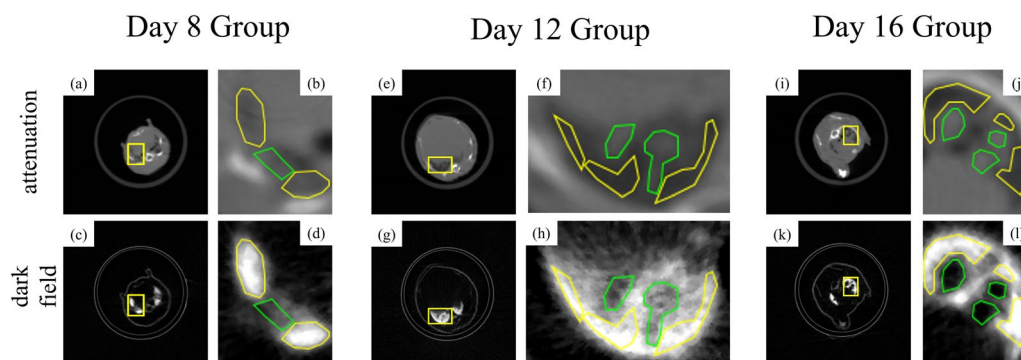


Fig. 4 Typical slices of attenuation and dark-field modality of the day 8 (a–d), day 12 (e–h), and day 16 (i–l) groups. For each group, a yellow rectangle was drawn on both images at the same place to mark the ROI, and the areas were zoomed and then median-filtered with a radius of 2 pixels. The green ROI indicates the nodules, while the yellow region of interest indicates the normal lung parenchyma

Table 2 Detectability index of attenuation and dark-field modality of lung nodules

Group	Imaging modality	Nodules		Normal pulmonary parenchyma		Detectability index
		Mean	SD	Mean	SD	
Day 8	Attenuation	0.517	0.039	0.500	0.039	0.436
	Dark-field	2.421	0.681	6.512	1.271	4.012
Day 12	Attenuation	0.434	0.044	0.311	0.028	3.335
	Dark-field	4.089	0.925	7.222	0.951	3.340
Day 16	Attenuation	0.558	0.030	0.368	0.061	3.953
	Dark-field	0.691	0.617	7.074	1.132	7.002

SD Standard deviation

Table 3 Detectability index of attenuation and dark-field modality measured in all the six mice with observable nodules

Group	Detectability index	
	Attenuation	Dark-field
Day 8	0.436	4.012
	3.728	4.626
Day 12	3.335	3.340
	6.557	7.529
Day 16	3.953	7.002
	4.172	6.524

Based on these indices, statistical analysis showed significantly ($p=0.025$) that dark-field modality outperforms attenuation in pulmonary nodule detection.

Autolysis analysis

The mice underwent pulmonary autolysis after euthanized [47]. To study the timing of autolysis, we evaluated the onset of pulmonary autolysis in healthy mice through histology. The results of this analysis are shown in Fig. 5. Dark spots are shown on autopsied lung tissue since 6 h

postmortem, and it can be observed that autolysis occurs at the location of the dark spots under microscope, which can be visualized on histological slices as erythrocyte leakage, and pyknosis of nuclei [48]. The erythrocyte leakage is indicated with a green arrow in Fig. 5i and h, and the pyknosis of nuclei can be determined by comparing the degree of nuclear staining at different time postmortem in Fig. 5e–h. Based on this analysis, we found that lung autolysis can be observed at 6 h after the death of the mice.

Considering the 8-h-long scan time of our CT, lung autolysis occurred during the experiment. As a result, the destruction of the alveoli structure during the experiment could have altered the dark-field signal and led to artifacts. To confirm whether our experiment was affected by autolysis, we compared the dark-field signal between the first and last several projections on one of the mice in day 4 group (Fig. 6). These projections were adjacent in angle but had a longer interval time. However, as shown in Table 4, the average dark-field signal fluctuated according to the angular position, which contradicted the possibility of autolysis where the dark-field signal would decrease in the experiment.

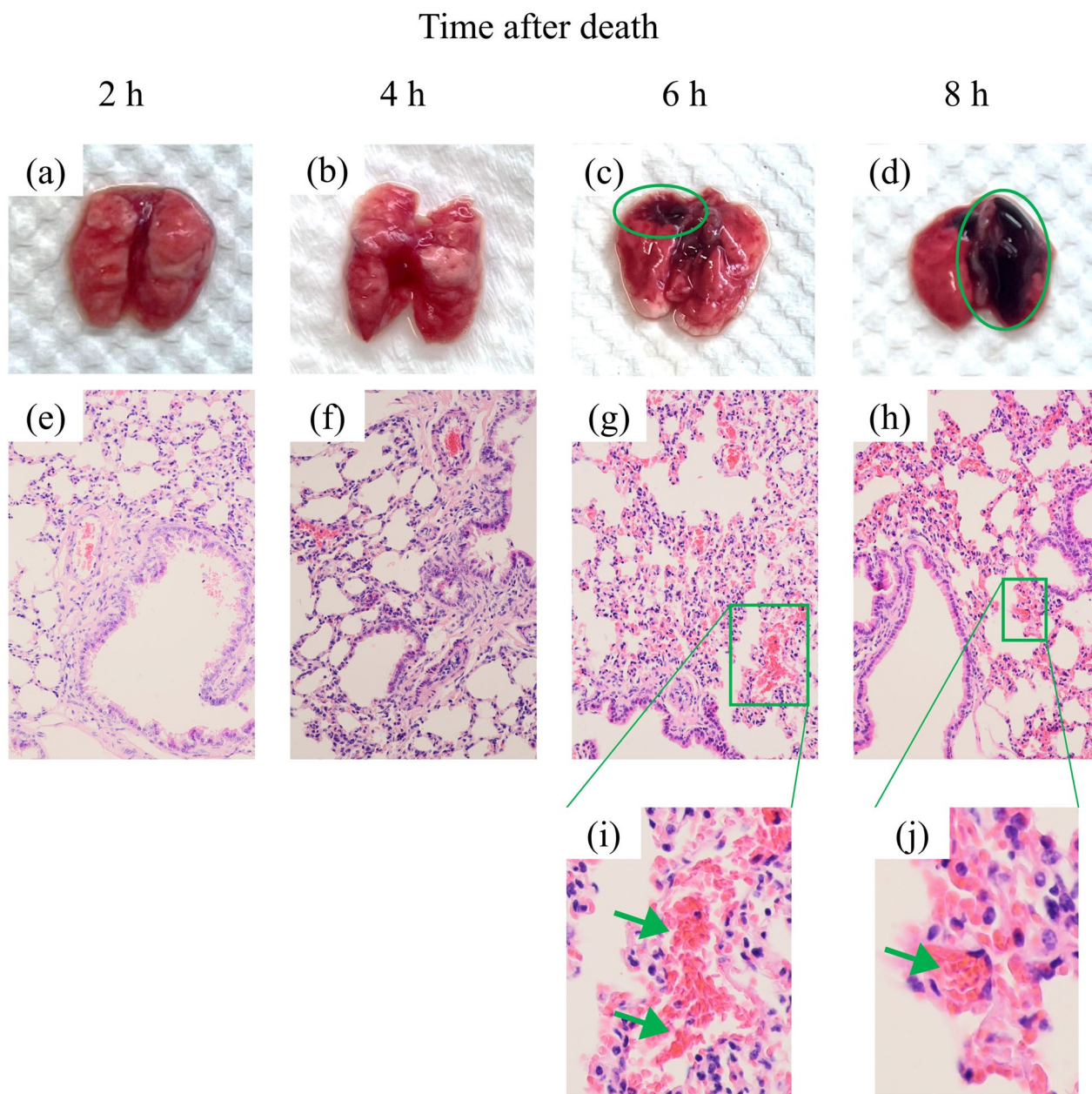


Fig. 5 The pulmonary autopsy (a–d) and pathological histology (e–h) of mice at 2, 4, 6, and 8 h after death. Pulmonary autolysis can be observed after 6 h. Dark spots (green ellipses) can be observed in autolysis results (c, d). Correspondingly, erythrocyte leakage can be observed in the histology results (g, h), which are zoomed in and marked with a green arrow in i and h

Statistical analysis was also conducted to further disprove the impact of autolysis. The pixels in ROIs of the first and last projections in Fig. 6 were selected, and one-sided paired *t*-test was applied to the dark-field signal of these two ROIs as mentioned above. *T*-test indicated significantly ($p=0.007$) that the dark-field signals in the last projection were not lower than those in the first projection, which showed that the dark-field signal in the same

position did not decrease during the experiment. Based on these findings, we concluded that lung autolysis had no significant impact on our experiment.

Discussion

In this study, we aimed to evaluate the feasibility of using dark-field CT to detect nodules at different stage of development using a lung cancer mouse model.

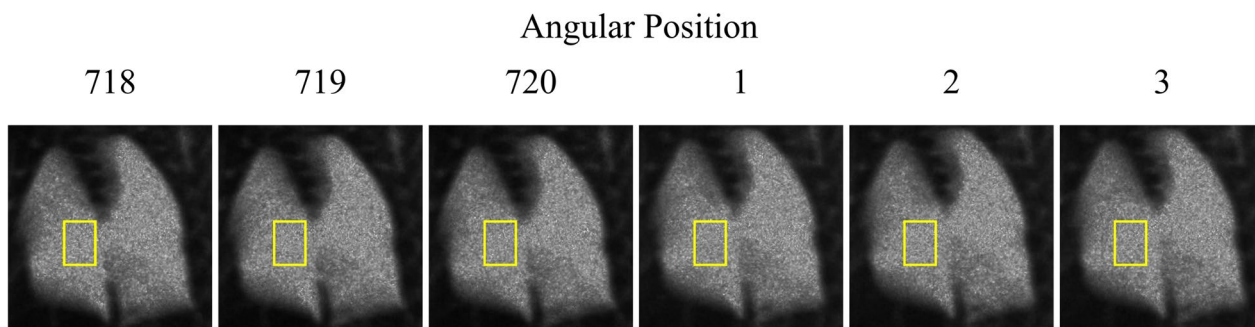


Fig. 6 The 718th to 720th and 1st to 3rd projection of one of the mice in the day 4 group. The yellow rectangle indicates the region of interest used to calculate the mean signal and standard deviation of the dark-field signal. The greyscale window was set between (0, 6.28)

Table 4 Mean and standard deviation of the dark-field signal of the region of interest drawn in Fig. 6 for the adjacent angular positions

Angular position	Mean	Standard deviation
718	3.356	0.504
719	3.376	0.486
720	3.343	0.466
1	3.312	0.462
2	3.371	0.477
3	3.306	0.480

Overall, our findings indicate that the dark-field modality complemented with the attenuation modality, and they revealed the micro-structural difference between nodules and normal pulmonary parenchyma. However, the dark-field modality exhibited a larger contrast between the pulmonary nodules and normal parenchyma. These findings were also confirmed by the quantitative analysis, which also showed that the lung nodule on the dark-field modality had a higher detectability index than the conventional attenuation modality after median filtering. This advantage was more pronounced in the day 8 group. These findings indicate that dark-field is better at detecting lung nodules at an early stage than the standard attenuation modality when the nodules are obvious in dark-field modality but not in attenuation modality.

We also conducted micro-CT to achieve high-resolution imaging for comparison and cross-validation with our dark-field CT. The acquisition time of our dark-field CT is longer than that of the micro-CT mainly due to the delay caused by mechanical movement and incompletely optimized data readout from the detector. However, micro-CT has several disadvantages. Although micro-CT has a better spatial resolution, it requires denser pixels for spatial resolution, thus producing a higher radiation

dose at the same statistical noise level [44]. Furthermore, image registration is hard to perform between micro-CT and dark-field modality due to different experimental setups, so it can only provide an approximate comparison, while in dark-field CT, the dark-field and attenuation modalities are retrieved from the same raw data captured by the detector, so these two modalities have an intrinsically perfect registration.

As for the above-mentioned abnormality of the day 12 group, the ground-glass opacity of the day 12 group in attenuation modality in Fig. 2e, m can be attributed to inflammation or blood vessel bursting. However, we could not compare the imaging findings with pathological data since pulmonary autolysis occurred after the death of the mice. Theoretically, ground-glass opacity represents the reduction of alveoli intervals, which will also lead to the reduction of dark-field signal. However, the signal of the two lungs has no obvious difference, while ground-glass opacity only exists in one of the two lungs. We attributed this finding to the reconstruction noise or low dark-field sensitivity of the current system.

Our current study has some limitations that have to be acknowledged. The limited hardware available and the large focal spot used in our study reduced the quality of the images. Several ring and radial artifacts were observed on tomographic images, which could be attributed to numerous factors, including non-uniform detector response, anisotropic scattering of the lung, phase stepping jitter, and focus drift. As shown in our quantitative study, since the dark-field signal is related to the visibility of the phase stepping curve, it is more sensitive to noise in the phase stepping than the attenuation modality. However, the use of median filtering in our study reduced the high-frequency noise in the reconstruction images, leading to an increase in the detectability index of dark-field modality. Besides, although each group consisted of two randomly selected mice, the potential influence of inherent confounding variables in mice is not

completely eliminated. Furthermore, due to the lack of histological analysis, the impact on diagnosis and treatment allocation by the improvement in detectability index of dark-field CT is so far unclear, which should be studied in the future work.

In our study, we had no strict control group, as all mice were inoculated with cancer. However, consistent with previous studies, no nodules were observed on the images on day 4 since the B16 cell lines started to produce cancer after 7 days. Therefore, no signal inhomogeneity was noted in the day 4 group.

Overall, we successfully used dark-field CT to monitor tumor progression in mice. Our findings suggest that dark-field CT might provide a promising, imaging modality to diagnose lung disease. This imaging modality could potentially improve diagnosis of lung diseases especially at early stage. Considering the latest development of dark-field CT prototype for human scale with scan times of 1 s [21], our long-term goal is to extend the lung disease diagnosis with dark-field CT to human scale.

Abbreviations

CT Computed tomography
ROI Region of interest

Authors' contributions

ZW (Tsinghua University) and YX conceptualized the study. PG, XZ (Tsinghua University), and CW conducted the dark-field CT experiments and analyzed the data. HZ conducted the micro-CT experiment. XZ (Peking Union Medical College) developed the mouse model. YX performed the histological assessment. PG and JL drafted the article manuscript. LZ, HY, ZW (Tsinghua University), and ZW (Capital Medical University) revised the manuscript. All authors read and approved the final manuscript.

Funding

This work was supported in part by National Natural Science Foundation of China (No.62227804), Tsinghua Precision Medicine Foundation (No.2022PY002), and Tsinghua University (Initiative Scientific Research Program, No. 20213080039 and 20221080066).

Availability of data and materials

The datasets used and analyzed during the current study are available from the corresponding author on reasonable request.

Declarations

Ethics approval and consent to participate

Institutional Review Board approval was obtained from Institute of Laboratory Animal Sciences, Chinese Academy of Medical Sciences (ZXW210001, 2021-04-12).

Consent for publication

Not applicable.

Competing interests

The authors declare that they have no competing interests.

Author details

¹Department of Engineering Physics, Tsinghua University, Beijing, China. ²Key Laboratory of Particle & Radiation Imaging (Tsinghua University) of Ministry of Education, Beijing, China. ³Institute for Precision Medicine, Tsinghua University, Beijing, China. ⁴School of Mathematical Sciences, Capital Normal

University, Beijing, China. ⁵NHC Key Laboratory of Human Disease Comparative Medicine, Beijing Engineering Research Center for Experimental Animal Models of Human Critical Diseases, Institute of Laboratory Animal Sciences, Chinese Academy of Medical Sciences (CAMS) and Comparative Medicine Center, Peking Union Medical College (PUMC), Beijing, China. ⁶Department of Radiology, Beijing Friendship Hospital, Capital Medical University, Beijing, China.

Received: 19 August 2023 Accepted: 20 October 2023

Published online: 25 January 2024

References

1. The top 10 causes of death. <https://www.who.int/news-room/fact-sheets/detail/the-top-10-causes-of-death>. Accessed 29 Dec 2022
2. Siegel RL, Miller KD, Fuchs HE, Jemal A (2022) Cancer statistics, 2022. *CA Cancer J Clin* 72:7–33. <https://doi.org/10.3322/caac.21708>
3. Torre LA, Siegel RL, Jemal A (2016) Lung cancer statistics. In: Ahmad A, Gadgeel S (eds) Lung cancer and personalized medicine: current knowledge and therapies. Springer International Publishing, Cham, pp 1–19
4. Quaderi SA, Hurst JR (2018) The unmet global burden of COPD. *Glob Health Epidemiol Genomics* 3:e4. <https://doi.org/10.1017/gheg.2018.1>
5. Sullivan J, Pravosud V, Mannino DM, Siegel K, Choate R, Sullivan T (2018) National and state estimates of COPD morbidity and mortality — United States, 2014–2015. *Chronic Obstr Pulm Dis* 5:324–333. <https://doi.org/10.15326/jcopdf.5.4.2018.0157>
6. Gassert FT, Urban T, Pfeiffer D, Pfeiffer F (2022) Dark-field chest radiography of combined pulmonary fibrosis and emphysema. *Radiol Cardiothorac Imaging* 4:e220085. <https://doi.org/10.1148/ryct.220085>
7. Dean M, Moitra K (2017) Biology of neoplasia. In: Thun M, Linet MS, Cerhan JR et al (eds) Cancer epidemiology and prevention. Oxford University Press, New York
8. Tsunoda S, Fukaya H, Sugihara T (1974) Lung volume, thickness of alveolar walls, and microscopic anisotropy of expansion. *Respir Physiol* 22:285–296. [https://doi.org/10.1016/0034-5687\(74\)90078-4](https://doi.org/10.1016/0034-5687(74)90078-4)
9. Kazerooni EA (2001) High-resolution CT of the lungs. *AJR Am J Roentgenol* 177:501–519. <https://doi.org/10.2214/ajr.177.3.1770501>
10. Weitkamp T, Diaz A, David C et al (2005) X-ray phase imaging with a grating interferometer. *Opt Express* 13:6296–6304. <https://doi.org/10.1364/OPEX.13.006296>
11. Weitkamp T, David C, Kottler C et al (2006) Tomography with grating interferometers at low-brilliance sources. In: Developments in X-ray tomography V. SPIE, pp 249–258. <https://doi.org/10.1117/12.683851>
12. Momose A, Takeda T, Itai Y, Hirano K (1996) Phase-contrast X-ray computed tomography for observing biological soft tissues. *Nat Med* 2:473–475. <https://doi.org/10.1038/nm0496-473>
13. Pfeiffer F, Bech M, Bunk O et al (2009) X-ray dark-field and phase-contrast imaging using a grating interferometer. *J Appl Phys* 105:102006. <https://doi.org/10.1063/1.3115639>
14. Pfeiffer F, Bech M, Bunk O et al (2008) Hard-X-ray dark-field imaging using a grating interferometer. *Nat Mater* 7:134–137. <https://doi.org/10.1038/nmat2096>
15. Gassert FT, Frank M, De Marco F et al (2022) Assessment of inflation in a human cadaveric lung with dark-field chest radiography. *Radiol Cardiothorac Imaging* 4:e220093. <https://doi.org/10.1148/ryct.220093>
16. Urban T, Sauter AP, Frank M et al (2023) Dark-field chest radiography outperforms conventional chest radiography for the diagnosis and staging of pulmonary emphysema. *Invest Radiol*. <https://doi.org/10.1097/RLI.0000000000000989>
17. Willer K, Fingerle AA, Noichl W et al (2021) X-ray dark-field chest imaging for detection and quantification of emphysema in patients with chronic obstructive pulmonary disease: a diagnostic accuracy study. *Lancet Digit Health* 3:e733–e744. [https://doi.org/10.1016/S2589-7500\(21\)00146-1](https://doi.org/10.1016/S2589-7500(21)00146-1)
18. Hellbach K, Baehr A, De Marco F et al (2018) Depiction of pneumothoraces in a large animal model using x-ray dark-field radiography. *Sci Rep* 8:2602. <https://doi.org/10.1038/s41598-018-20985-y>
19. Jud C, Braig E, Dierolf M et al (2017) Trabecular bone anisotropy imaging with a compact laser-undulator synchrotron x-ray source. *Sci Rep* 7:14477. <https://doi.org/10.1038/s41598-017-14830-x>

20. Michel T, Rieger J, Anton G et al (2013) On a dark-field signal generated by micrometer-sized calcifications in phase-contrast mammography. *Phys Med Biol* 58:2713–2732. <https://doi.org/10.1088/0031-9155/58/8/2713>
21. Viermetz M, Gustschin N, Schmid C et al (2022) Dark-field computed tomography reaches the human scale. *Proc Natl Acad Sci* 119:e2118799119. <https://doi.org/10.1073/pnas.2118799119>
22. Schaff F, Malecki A, Potdevin G et al (2014) Correlation of x-ray vector radiography to bone micro-architecture. *Sci Rep* 4:3695. <https://doi.org/10.1038/srep03695>
23. Wiczorek M, Schaff F, Jud C et al (2018) Brain connectivity exposed by anisotropic x-ray dark-field tomography. *Sci Rep* 8:14345. <https://doi.org/10.1038/s41598-018-32023-y>
24. Scherer K, Yaroshenko A, Böllükbas DA et al (2017) X-ray dark-field radiography - in-vivo diagnosis of lung cancer in mice. *Sci Rep* 7:402. <https://doi.org/10.1038/s41598-017-00489-x>
25. Taphorn K, Mechlem K, SELLERER T et al (2021) Direct differentiation of pathological changes in the human lung parenchyma with grating-based spectral x-ray dark-field radiography. *IEEE Trans Med Imaging* 40:1568–1578. <https://doi.org/10.1109/TMI.2021.3061253>
26. Velroyen A, Yaroshenko A, Hahn D et al (2015) Grating-based x-ray dark-field computed tomography of living mice. *EBioMedicine* 2:1500–1506. <https://doi.org/10.1016/j.ebiom.2015.08.014>
27. Burkhardt R, Gora T, Fingerle AA et al (2021) In-vivo x-ray dark-field computed tomography for the detection of radiation-induced lung damage in mice. *Phys Imaging Radiat Oncol* 20:11–16. <https://doi.org/10.1016/j.phro.2021.09.003>
28. Fidler IJ, Kripke ML (1977) Metastasis results from preexisting variant cells within a malignant tumor. *Science* 197:893–895. <https://doi.org/10.1126/science.887927>
29. Yashiro W, Terui Y, Kawabata K, Momose A (2010) On the origin of visibility contrast in x-ray Talbot interferometry. *Opt Express* 18:16890–16901. <https://doi.org/10.1364/OE.18.016890>
30. Momose A, Kawamoto S, Koyama I et al (2003) Demonstration of x-ray Talbot interferometry. *Jpn J Appl Phys* 42:L866. <https://doi.org/10.1143/JJAP42.L866>
31. Pfeiffer F, Weitkamp T, Bunk O, David C (2006) Phase retrieval and differential phase-contrast imaging with low-brilliance x-ray sources. *Nat Phys* 2:258–261. <https://doi.org/10.1038/nphys265>
32. Wang Z-T, Kang K-J, Huang Z-F, Chen Z-Q (2009) Quantitative grating-based x-ray dark-field computed tomography. *Appl Phys Lett* 95:094105. <https://doi.org/10.1063/1.3213557>
33. Chen G-H, Bevins N, Zambelli J, Qi Z (2010) Small-angle scattering computed tomography (SAS-CT) using a Talbot-Lau interferometer and a rotating anode x-ray tube: theory and experiments. *Opt Express* 18:12960–12970. <https://doi.org/10.1364/OE.18.012960>
34. Strobl M (2014) General solution for quantitative dark-field contrast imaging with grating interferometers. *Sci Rep* 4:7243. <https://doi.org/10.1038/srep07243>
35. Malecki A, Potdevin G, Biernath T et al (2013) Coherent superposition in grating-based directional dark-field imaging. *PLoS One* 8:e61268. <https://doi.org/10.1371/journal.pone.0061268>
36. Malecki A, Potdevin G, Biernath T et al (2014) X-ray tensor tomography. *EPL - Europhys Lett* 105:38002. <https://doi.org/10.1209/0295-5075/105/38002>
37. Bayer F, Zabler S, Brendel C et al (2013) Projection angle dependence in grating-based X-ray dark-field imaging of ordered structures. *Opt Express* 21:19922–19933. <https://doi.org/10.1364/OE.21.019922>
38. Momose A, Yashiro W, Harasse S, Kuwabara H (2011) Four-dimensional X-ray phase tomography with Talbot interferometry and white synchrotron radiation: dynamic observation of a living worm. *Opt Express* 19:8423–8432. <https://doi.org/10.1364/OE.19.008423>
39. Oppelt A (2006) Imaging systems for medical diagnostics: fundamentals, technical solutions and applications for systems applying ionizing radiation, nuclear magnetic resonance and ultrasound, 2nd edn. Publicis, Erlangen
40. Conrad. <https://www5.cs.fau.de/conrad/>. Accessed 12 Dec 2022
41. Feldkamp LA, Davis LC, Kress JW (1984) Practical cone-beam algorithm. *JOSA A* 1:612–619. <https://doi.org/10.1364/JOSAA.1.000612>
42. Sharp P, Barber DC, Brown DG, et al (1996) Report 54. *JICRU os28:NP-NP*. <https://doi.org/10.1093/jicru/os28.1.Report54>
43. Samei E, Bakalyar D, Boedeker KL et al (2019) Performance evaluation of computed tomography systems: summary of AAPM Task Group 233. *Med Phys* 46:e735–e756. <https://doi.org/10.1002/mp.13763>
44. Barrett HH, Myers KJ (2013) Foundations of image science. Wiley, New York
45. Goulden CH (1959) Methods of statistical analysis, 2nd edn. Wiley, New York
46. MacMahon H, Naidich DP, Goo JM et al (2017) Guidelines for management of incidental pulmonary nodules detected on CT images: from the Fleischner Society 2017. *Radiology* 284:228–243. <https://doi.org/10.1148/radiol.2017161659>
47. Bachofen M, Weibel ER, Roos B (1975) Postmortem fixation of human lungs for electron microscopy. *Am Rev Respir Dis* 111:247–256. <https://doi.org/10.1164/arrd.1975.111.3.247>
48. Ilse G, Kovacs K, Ryan N, Horvath E, Ilse D (1979) Autolytic changes in the rat adenohypophysis: a histologic, immunocytologic and electron microscopic study. *Exp Pathol (Jena)* 17:185–195. [https://doi.org/10.1016/S0014-4908\(79\)80011-3](https://doi.org/10.1016/S0014-4908(79)80011-3)

Publisher's Note

Springer Nature remains neutral with regard to jurisdictional claims in published maps and institutional affiliations.